Analysis of the load exerted by debris flows on filter barriers: Comparison between numerical results and field measurements

Analysis of the load exerted by debris flows on filter barriers: comparison between numerical results and field measurements

Alessandro Leonardi[a], Marina Pirulli[a]

[a]*Politecnico di Torino*
Department of Structural, Geotechnical, and Building Engineering
24 Corso Duca degli Abruzzi, Turin, Italy

Abstract

The hazard posed by debris flows onto mountainous settlements often requires structural countermeasures, such as barriers, to be installed. There is a worldwide trend in employing barriers that are partially impervious to the flow, trapping the coarsest sediment, and reducing the erosive power of the flow early on. However, many design choices with respect to effectiveness and structural integrity are not trivial, because there is a poor knowledge of the flow-structure interaction mechanism. In this work, we report results from a monitoring campaign on a barrier installed within an experimental site. At the site, the structural response of the barrier is recorded any time an event occurs. However, the results exhibit features that do not fully reconcile with the load model prescribed by the available guidelines. To gather insight, we propose a numerical study based on the use of the Discrete Elements Method for the flow simulation and the Finite Element Method for the structural response of the barrier. The compatibility between site measurements and numerical output validates the use of the DEM-FEM model. It also highlights certain key details on the load pattern on the barrier that are not yet included in existing guidelines.

Keywords: Debris flow, filter barrier, site monitoring, numerical modelling, discrete element method

1. Introduction

Steep creeks in mountainous terrains are subject to hazards such as debris flows (Hungr et al., 2001; Petley, 2012). These count among the most dangerous natural events, posing a constant threat to settlements on mountainous terrain and considerably handicapping the design and maintenance of infrastructures (Hungr and Jakob, 2005). Debris flows are typically rich in coarse sediment, and can induce significant bed erosion and entrainment. This inflates the amount of flowing material, in turn leading to growing erosive power (Pirulli and Pastor, 2012).

To check the hazard related to this feedback mechanism, dams and barriers are often installed in the catchment. The recent years have seen a growing use of barriers with a certain degree of permeability (filter barriers), thus retaining only a fraction of the flowing mass. These barriers are often designed to retain the coarsest debris by inducing partial or total jamming at the outlets (Piton and Recking, 2016). At the same time, they allow fine sediments, which have reduced erosion potential and can be more easily conveyed and dosed, to filter downstream. These designs are a compromise between the need to trap sediments and break the energy of the flow, and the requirement to keep maintenance work as low as possible. This determines a lower maintenance cost and environmental impact with respect to impervious barriers. Example of structures of this type are provided in Fig. 1: one or multiple outlets are present. In these cases, the interaction mechanism between flow and structure is not trivial: the barrier, while breaking the energy of the flow, also induces an alteration of pore pressure, and an activation of inter-particle friction (Song et al., 2018; Cabrera and Estrada, 2019).

The impact of a mass characterized by a significant content of grains on an impervious barrier has been extensively studied (e.g. Albaba et al., 2015; Gabrieli and Ceccato, 2016; Calvetti et al., 2019). However, it is not clear whether the results of these studies can also be extensively applied to filter barriers. From recent studies (e.g. Leonardi et al., 2019), it emerges that the presence of an outlet can induce accumulation of stresses, which can further complicate the estimation of the maximum expected load. This makes a rational design, both for performance and structural integrity, problematic. Additionally, few design prescriptions and guidelines are available worldwide. Here we refer to the Austrian guideline series ONR 2480X (Rudolf-Miklau and Suda, 2011), and to the set of guidelines developed in Hong Kong (Kwan, 2012). The former recommends to estimate the impact pressure with a formula based on a combination of momentum exchange and gravitational load (Suda et al., 2012). The latter recommends a pressure proportional to the square of the front velocity. In both approaches, the dynamic load is considered uniform across the barrier surface.

These guidelines do not directly consider jamming, i.e. that the outlets can clog through the formation of granular arches (Janda et al., 2008; Chevoir et al., 2007). The load distribution on the barrier is assumed to act only in the direction of the incoming flow (Hübl et al., 2009; Kwan, 2012). The consequences of this simplification have not yet been completely explored. From small-scale experiments, it is clear that mo-

Figure 1: Examples of debris flow mitigation structures, with energy-breaking or filtering function. (a) Front breakers and (b) slit-filter barrier installed in Pollein, Aosta Valley, Italy. (c) Flexible steel-ring net installed in Bussoleno, Piedmont, Italy. (d) Debris-resisting baffles near Yu-Thung Road, Hong Kong, HKSAR.

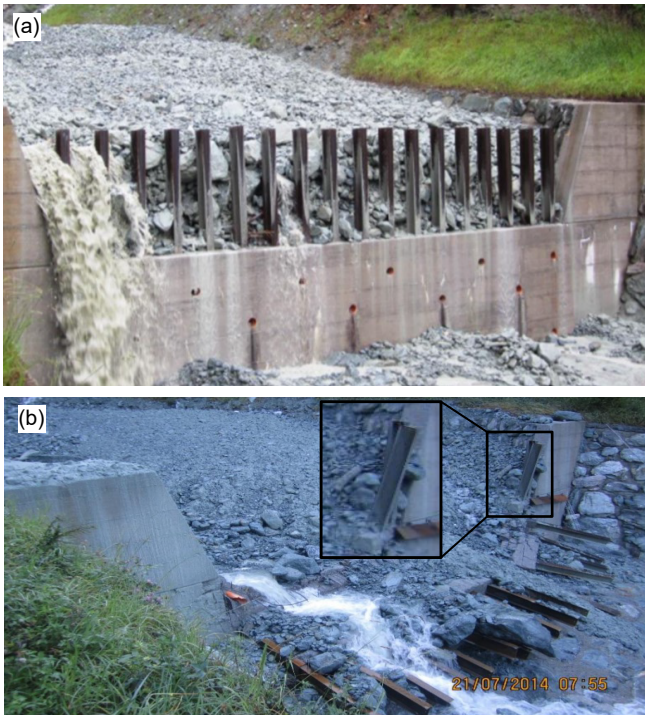

Figure 2: The filter barrier installed in the Grand Valey experimental site. (a) Picture of the intact barrier and (b) immediately after the collapse in 2014. Pictures courtesy of the Aosta Valley Regional Government.

mentum transfer in the direction parallel to the mean flow is the main source of load (e.g. Canelli et al., 2012; Koo et al., 2017). However, granular material close to the jamming transition can exert forces with intensity and directions that are not easily predictable (Bharadwaj et al., 2006; Hidalgo et al., 2013). If not correctly accounted for, this could potentially lead to premature failure of a barrier, or to damage that reduces its operational capacity.

To investigate the type of interaction occurring between filter barriers and boulder-rich debris flows, an experimental site has been set up in the municipality of St.Vincent, Western Italian Alps (Pirulli et al., 2014a). The site is prone to the release of multiple debris flows every year, and contains the barrier shown in Fig. 2(a). A monitoring station records the load induced on the barrier whenever it is impacted by a flow.

The barrier experienced a sudden collapse on the 20th of July 2014 during a minor event, see Fig. 2(b). In that instance, the deposition basin was partially filled by a previous event, and the surge that caused the collapse likely completely obstructed the barrier, causing significant overflow. This event was not particularly intense, and the barrier should have in principle responded without deteriorating. This highlighted how our understanding of the interaction between flow and structure, and specifically of the patterns of load transfer, should be further deepened.

In this paper, we aim to understand the exact type of load transmitted to structures where clogging can occur, and the consequences on the design choices. We do this by reporting and analyzing recordings from the monitored barrier in St. Vincent. Since no recordings exist of the 2014 event, the investigation of the collapse causes remain out of the scope of this paper. Instead, a single well-documented event is chosen as benchmark for numerically back-calculating the interaction between barrier and flow. We employ a numerical model, which, in spite of numerous necessary simplifications, is able to describe the most relevant features of the phenomenon. The debris mass is simulated with the Discrete Element Method (DEM), which allows to comprehensively reconstruct the type of load exerted by a front rich of coarse grains. The DEM model provides a three-dimensional picture of the interaction between a coarse granular front and the barrier. As a second step, we plug the obtained load into a Finite Element Model (FEM). Through dynamic transient analyses, we obtain the structural response on the barrier that corresponds to the front impact.

The paper is organized as follows. We firstly describe the

experimental site and the collected datasets. We proceed by outlining the DEM-FEM framework adopted for the back analysis. Subsequently, we show how the numerical procedure reconstructs a load pattern that is compatible with the recordings obtained on site. Using this approach, we compute a more realistic multi-surge sequence of impacts on the barrier, which describes a typical event in the monitored basin. We describe the obtained load pattern, and determine in which regards the DEM-FEM model provides a more conservative estimation of the impact load compared to reference design guidelines. Based on these results, we provide a set of suggestions that aim at improving the design of this type of barriers, and of effective monitoring systems.

2. The Grand Valey experimental site

2.1. Site description

The site used as study-case in this work is located in the municipality of St. Vincent, within the Aosta Valley Autonomous Region, Italy (see Fig. 3). The settlement is partially located on the deposition fan of the Grand Valey creek, which drains an area of 5.22 km^2, at an altitude between 700 m and 2719 m a.s.l., the highest point being Mount Zerbion.

The mean slope of the creek bed is 38%, which decreases to 12% on the alluvial fan. Close to the hamlet of Perrière, at an altitude of about 1150 m a.s.l., the creek branches into two channels, labeled A and B in Fig. 3. Both branches drain a part of the basin that is characterized by steep slopes at high altitude, composed of heavily fractured schists with subordinate phyllitic levels, serpentinite, and prasinites metagabbros. These slopes are only partially covered by vegetation and are prone to be easily eroded by heavy or moderate rains, such as those routinely recorded during spring and summer. The combination of these factors makes both branches prone to the release of debris flows with annual frequency. Similar conditions can be encountered in certain sites in the Italian Dolomites (Tecca and Genevois, 2009) and in the Pyrenees (Pastorello et al., 2018).

A list of all documented events from 2004 to the present day is provided in Table 1. A debris flow in 2004 reached the settlement of St. Vincent, causing limited damage but, at the same time, highlighting hazard exposure. The sequence of events in 2008 heavily damaged the barriers installed in the main channel, with debris reaching the alluvial fan in proximity to the settlement. This prompted a general revision of the hazard management techniques by the local government (Pirulli et al., 2014a). To reduce the risk associated with future events, a sequence of structural countermeasures was therefore installed, and available structures were upgraded. The goal was to reduce the amount of debris that reaches the lowest part of the basin, and in particular to retain the coarsest sediments as upstream as possible. The site now features two filter barriers (at location 1 in Fig. 3), three steel-ring nets (at location 2), and a slit dam (location 3).

2.2. Countermeasures

The two filter barriers are located immediately after the confluence of the two branches, on a section with a gentle slope (around 12°). This is directly below the steep slopes responsible for the mobilization of coarse material (A2 and B1 in Fig. 3). The barriers are essentially rack structures, built by inserting a sequence of slender steel bars on a concrete basement. They are routinely hit by flows with relatively small volume (usually a few thousand cubic meters), surging through multiple consecutive impulses and with a high content of coarse grains. One of the filter barriers, the first impacted by flows, is shown in Fig. 2(a).

Each barrier (Fig. 4) features a sequence of eighteen steel I-beams (IPE 270), with spacing $i = 0.6$ m, mounted on a concrete basement. Between two consecutive beams, an outlet with transverse size $S = 0.47$ m is present. The two structures, including the lateral wings, span the whole width of the channel (17 m), and are separated by a retention basin 46.5 m long. Together, they can retain about 5000 m^3 of debris. They are designed to filter out the coarse grains, inducing deposition in the retention basin, while allowing fines and water to flow downstream. This system requires regular maintenance: the basin

Table 1: The main documented debris flow events in the Grand Valey basin.

2004		**2008**		**2009**	
Date	Volume [m^3]	Date	Volume [m^3]	Date	Volume [m^3]
07/08	3000	28/05	6400	26/05	10000
		12/07	3500		
		06/09	5000		
		03/11	3000		
2011		**2012**		**2013**	
Date	Volume [m^3]	Date	Volume [m^3]	Date	Volume [m^3]
06/06	3975	29/08	3975	17/07	3550
16/06	200			29/07	3810
17/06	300				
22/06	500				
13/07	4500				
26/08	4500				
2014		**2015**		**2016**	
Date	Volume [m^3]	Date	Volume [m^3]	Date	Volume [m^3]
06/06	2790	19/03	800	09/06	1875
12/06	2090	08/06	5000	11/07	4420
07/07	4670	14/08	2000		
20/07	4625				
23/07	2565				
03/08	725				

Table 2: Geometrical parameters of the IPE 270 section, and sensor position. Refer to Fig. 6 for a graphical reference.

Width h_x [mm]	135
Height h_y [mm]	270
Sensor distance from x axis s_x [mm]	35
Sensor distance from y axis s_y [mm]	135
Inertia moment (x axis) I_{xx} [mm^4]	$420 \cdot 10^4$
Inertia moment (y axis) I_{yy} [mm^4]	$5790 \cdot 10^4$

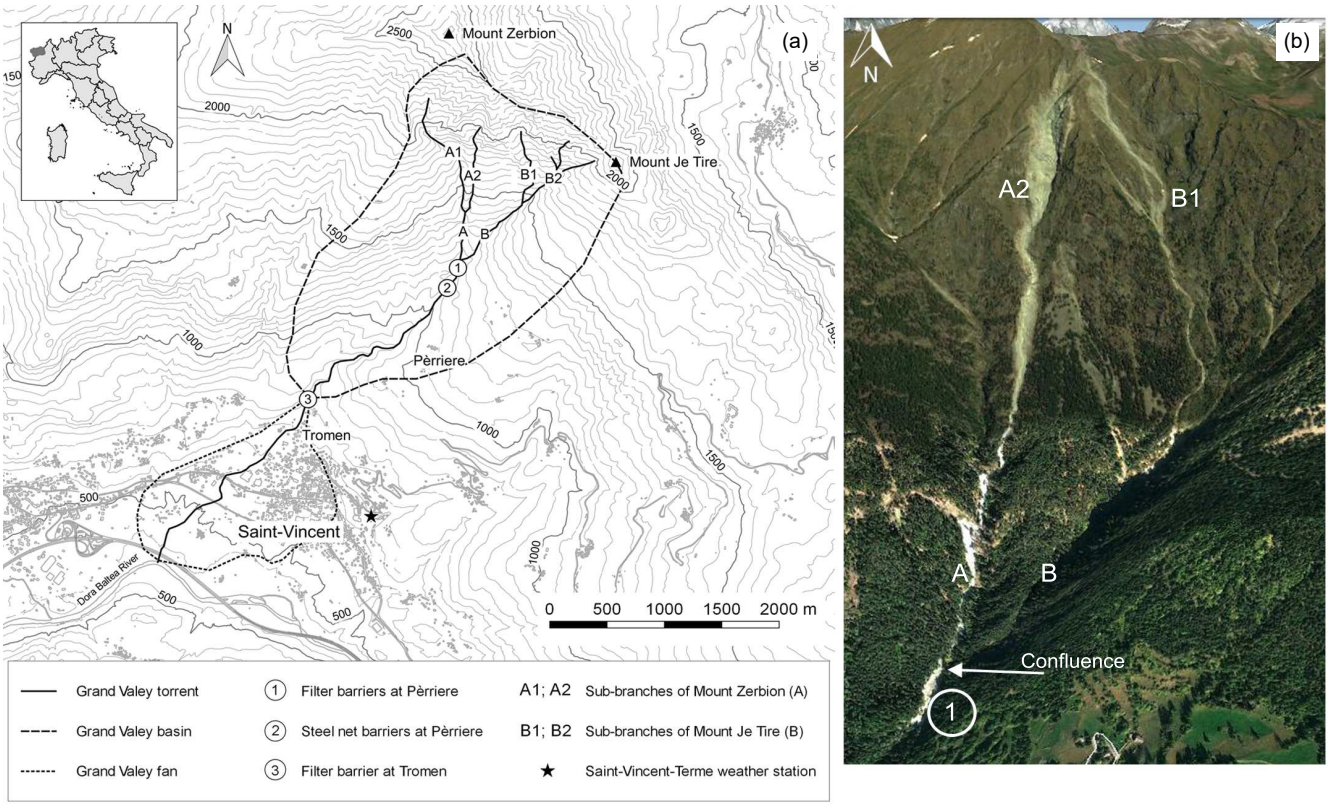

Figure 3: The basin drained by the Grand Valey torrent. (a) topography of the catchment and location of the countermeasures. (b) Aerial picture showing the branches that are the major source of coarse sediment.

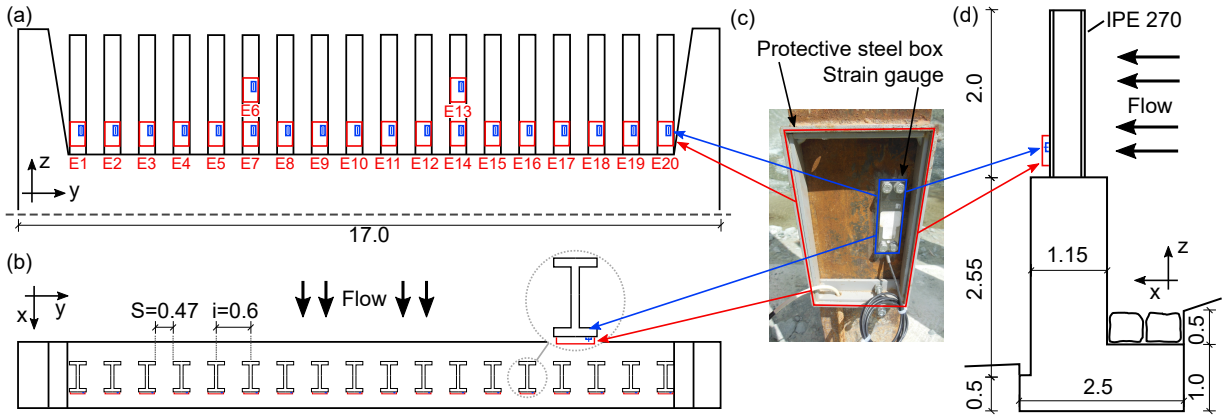

Figure 4: Schematic of the monitored barrier in the Grand Valey experimental site: (a) front view (b) top view, and (d) lateral section of the barrier, with the location of the boxes containing the extensometers. Each box is labelled with the progressive number of the installed extensometer, e.g. E4 contains extensometer number 4. Sizes are expressed in meters. (c) Picture of an open box, showing the location of the SLB-700A extensometer installed on a bar flange.

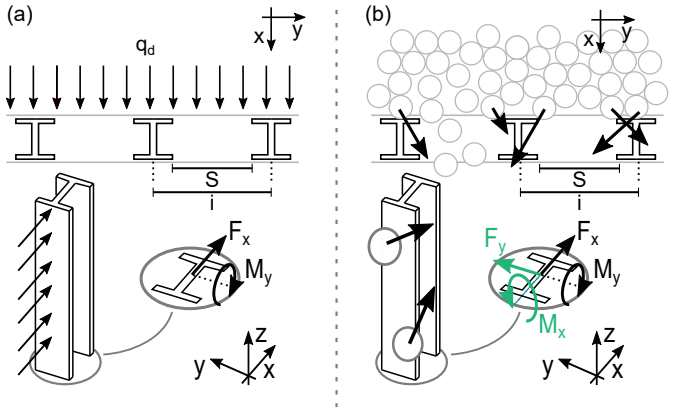

Figure 5: The load prescribed by the available guidelines, commonly used to design filter structures. (b) The load pattern proposed in this work to back-calculate the site recordings.

needs to be emptied after every major event in order to restore its effectiveness.

Following Pirulli et al. (2014a), the barrier is designed to withstand a dynamic load computed, per unit area, as

$$q_d = k\rho_b v_f^2 \tag{1}$$

with ρ_b being the bulk density of the debris material, v_f the front speed, and k an empirical coefficient.

The design load is assumed to be uniformly distributed along the barrier surface, as illustrated in Fig. 5(a). The structural response of each bar is therefore supposed to be equivalent to a vertical cantilever, subject to uniaxial bending. Following this scheme, and the reference system introduced in the figure, the bar section at the joint with the basement is subject to a shear force F_x and a (negative) bending moment M_y. The barrier was originally designed to resist flows with mean front speed up to 5m/s.

The design proved to not be sufficiently conservative. On the 20th of July 2014, the first barrier impacted by the flow completely collapsed. The premature failure was probably due to deficiencies in structural details, and in particular to inadequate reinforcement of the concrete basement. However, it was noted that the bars had deformed significantly (see the inset in Fig. 2 (b)). This suggested that the load scheme described in Fig. 5(a) needed to be reviewed. For this reason, the newly built barrier was equipped with an improved monitoring system. The data collection procedure is described in the following section.

3. Site recordings and interpretation

The aftermath of the 2014 collapse is shown in Fig. 2(b). The barrier was rebuilt in 2015 following the schematic illustrated in Fig. 4. The full characterization of the recordings obtained so far, and their correlation with the type of events occurring in the basin, is beyond the scope of this work, and will be presented in a separate paper. Here, we briefly describe the type of data acquired, and focus on a sample of recordings to use for the interpretation of the flow-structure interaction behavior.

The system is peculiar because the load is not measured directly. Rather, it is inferred by measuring the structure deformation, and specifically by tracking the deformation of the structural elements with filtering functions, i.e. the steel bars (Pirulli et al., 2014b). This allows to avoid installing instrumentation that interacts directly with the flow, which can be easily subject to wearing and damage.

This strategy is therefore reliable and cost-efficient, although it requires an understanding of how the barrier deforms when loaded. In the literature, examples of this approach are found in Wendeler and McArdell (2006), where the stress induced on a flexible steel-ring net is measured, or in Luis-Fonseca et al. (2011). More commonly, experimental sites employ devices that are placed in contact with the debris material, and that measure the loads directly. Examples of monitoring stations that follows this strategy are found in Japan (Suwa et al., 2011), the United States (Coe et al., 2008; McCoy et al., 2010), France (Navratil et al., 2013), Austria (Kogelnig et al., 2014), Italy (Marchi et al., 2002; Comiti et al., 2014), Spain (Hürlimann et al., 2011), and Switzerland (Hürlimann et al., 2003; McArdell et al., 2007; Berger et al., 2011). To our extent of knowledge, the monitoring system in St. Vincent is the only case reported in the literature where the impact of real events are directly measured on a rigid filter barrier.

Each steel bar is equipped with one or more extensometers (HBM SLB-700A), as described in Fig. 4. The devices consist of a metallic box containing four electric strain gauges mounted on a metallic plate with size $84 \times 25.4 \times 6.4$ mm. The system self-balances the dilation induced by thermal strains, and operates effectively in a temperature between -20°C and 60°C (Borri-Brunetto et al., 2016). The extensometers are designed to record the local axial strain (ε_z) at the position where they are mounted, i.e. close to the joint between the downstream flange and the concrete basement (except for E6 and E13, which are located mid-height). The extensometers record up to a nominal strain of $\pm 500\mu$m/m. The controller acquires the strain measurements from the gauges at time intervals of 1.15 s (0.87 Hz) and stores data every 10 minutes on a removable solid-state drive. The axial strain is considered positive if the fibers are stretched and negative if they are compressed.

The flanges that host the extensometers undergo compression when loaded from upstream, i.e. by a bending moment M_y (Fig. 6). According to the Euler-Bernoulli theory, this induces a strain equal to

$$\varepsilon_z = -\frac{M_y}{EI_{yy}} s_y \tag{2}$$

with E the Young's modulus of structural steel, I_{yy} the moment of inertia of the bar section in the plane of the web and s_y the distance of the strain gauge from the strong axis y (see Fig. 6 and Table 2).

The system in St. Vincent allows an estimate of the intensity, frequency and temporal evolution of the phenomena. The recordings however show a counterintuitive distribution of stresses, which does not reconcile with the traditional load patterns prescribed by the aforementioned guidelines. Under the uniaxial load pattern described in the Fig. 5(a) and Eq. 2, the

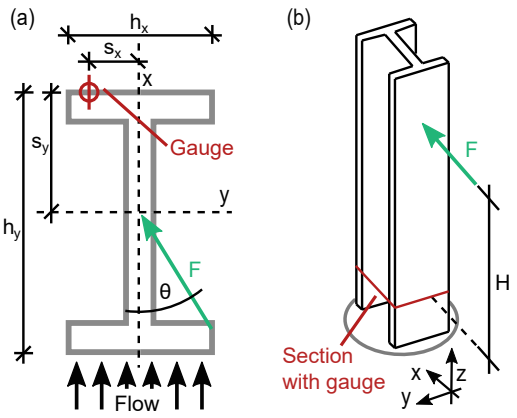

Figure 6: (a) Section and (b) axonometric projection of the bar, with location of the strain gauge (not to scale), and identification of the local reference system. For the section geometrical characteristics, refer to Table 2

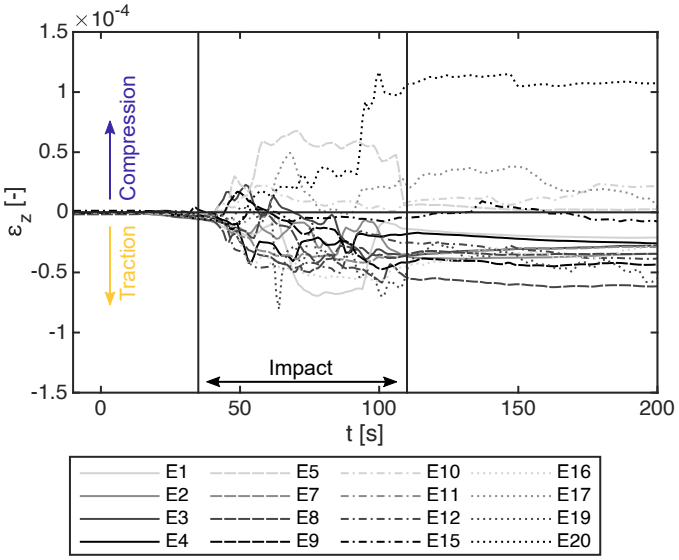

Figure 7: Strains recorded during the June 9th 2016 event. Each line corresponds to the output of one of gauge from the lowest set. Extensometers E6 and E13 are not directly comparable to the other ones, being located at a different height. Therefore, they are excluded from the analysis. Extensometers E14 and E18 were malfunctioning, and did not report a signal. The graph highlights the impact phase, i.e. the time when the load on the barrier has not stabilized yet.

extensometers were originally expected to record only negative strains (i.e. compression). However, this proved not to be the case. The strains recorded during the June 9th 2016 event by all the lower sensors are shown in Fig. 7. While many sensors only record compression, as expected, there is a significant number of sensors that record positive strain, i.e. undergo traction. Certain sensors also experience rapid shifts in magnitude, and sudden changes from traction to compression and vice-versa.

Explaining the origin of this behavior from the recordings alone is difficult. Inertial loads, such as those induced by the bar oscillations after a momentous impact, could account for short-lived traction stresses on the flanges. However, positive strains often endure, and some persist even when the system stabilizes after the surge front has passed. Therefore, two explanations appear as reasonable: (i) the flow hits the barrier in a direction that is non-orthogonal, or (ii) there exist significant off-plane load components due to the interaction of large grains with the bars. Both cases assume the existence of an off-plane bending moment M_x, as illustrated in Fig. 5(b). This secondary component should have an intensity sufficient to significantly influence the strain induced on the sensors. If this is true, Eq. 2, should be rewritten considering bi-axial bending as:

$$\varepsilon_z = \frac{M_x}{EI_{xx}} s_x - \frac{M_y}{EI_{yy}} s_y \tag{3}$$

with I_{xx} the moment of inertia of the bar section out of the plane of the web and s_x the distance of the strain gauge from the weak axis of the bar section x (see Fig. 6 and Table 2). Unfortunately, this implies that one value of ε_z is related to two bending moments M_x and M_y. It is therefore impossible to reconstruct the load pattern without further assumptions, e.g. by assuming a specific load direction $\theta = \text{atan}(-M_x/M_y)$.

The hypothesis of a flow that hits the barrier from a uniform non-orthogonal direction θ would determine recordings that cross-correlate over multiple bars. Oppositely, the recordings in Fig. 7 show an erratic behavior. Therefore, it seems reasonable to hypothesize that the compressive strains are principally due to the discrete nature of the load, imputable to the presence of large grains on the front. To test this, we set up a numerical model, and use it to simulate the interaction in controlled conditions.

4. DEM-FEM approach for the simulation of flow-barrier interaction

4.1. DEM model for the flow front

The staggering complexity of debris materials requires the adoption of a simplified approach for the simulation. Here, we test the hypothesis that coarse grains are responsible for the counterintuitive deformation pattern recorded on the barrier. Therefore, the presence of a fluid phase and of fine sediments is for the moment neglected. This has strong implications on other aspects of the flow-structure interaction. In particular, it bypasses the important role of changes in pore fluid pressure, which can strongly influence grain mobility (Kaitna et al., 2016). Note that even a multi-phase method would not be able

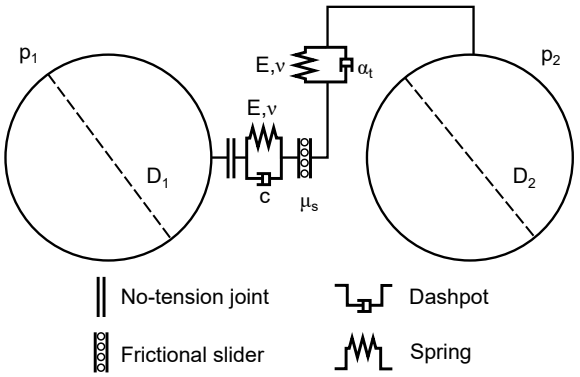

Figure 8: Schematics of the DEM contact model and of the physical meaning of the simulation parameters. Adapted from Marchelli et al. (2019).

to fully represent the real grain-size distribution at the site scale. Thus, a rigorous treatment of debris material in this context remains beyond the reach of current state-of-the-art methods.

We therefore adopt a strategy based solely on the application of DEM for the flow simulation. This method treats the debris mass as an assembly of spherical particles. This has two important consequences. Firstly, with DEM there is a strong limitation on the number of grains that can be modeled. Secondly, the use of spherical particles implies that interlocking effects due to non-spherical shapes cannot be explicitly described. From Iverson (2015), we know that an assembly of spheres is less compressible compared to an assembly of angular particles. Furthermore, the clogging probability can be severely altered by particle anisotropy (Ashour et al., 2017). The addition of rolling resistance to the contact model (as described below) partially addresses this issue (Marchelli et al., 2019). In spite of these necessary simplifications, DEM remains to date the most comprehensive and commonly used tool capable of reproducing the interaction between a mass composed of large grains and solid obstacles (Bharadwaj et al., 2006; Albaba et al., 2015), especially when a jamming transition occurs (Albert et al., 2000; Leonardi et al., 2019).

It should be noted that numerical methods based on a continuum approach, such as the Lagrangian finite elements (Kwan et al., 2015), the material point method (Llano-Serna et al., 2016), fictitious-domain fluid solvers (Cheng et al., 2018), the lattice-Boltzmann method (Leonardi et al., 2015; Ding and Xu, 2018), or smoothed particle hydrodynamic (Dai et al., 2017; Huang et al., 2012) are also suitable for reconstructing the fluid-structure interaction. However, they rely on an equivalent-fluid description of the material, effectively smoothing the effect of discrete loads induced by particles (Ceccato et al., 2018). Furthermore, these methods cannot simulate granular jamming. They are therefore inappropriate for the simulation of granular clogging.

The DEM solver used here is based on the code by Leonardi et al. (2016), with the modified contact model described by Marchelli et al. (2019). The reader is redirected to those works for the full theoretical background, the code layout, and a definition of the simulation parameters listed in the following sections.

The contact model is schematically represented in Fig. 8. The particle elastic properties are defined with a Young's modulus E and a Poisson coefficient ν. The contact model employs a non-linear damped Hertzian law for the normal component of the collision force (Pöschel and Schwager, 2005). The dissipation is adjusted in order to obtain a constant coefficient of restitution, as in Tsuji et al. (1992). In the tangential direction, contacts are frictional with a coefficient of static friction μ_s. The frictional behavior is implemented using elastic springs as in Luding (2008). The tangential spring stiffness, in analogy to the contact model in the normal direction, is determined by E and ν. Relative rotation of colliding particles is subject to an additional dissipation source. Following Marchelli et al. (2019), this is implemented with a rolling resistance mechanism, whose intensity is governed by a dimensionless rolling coefficient μ_r. With this model, grains can spontaneously jam, clogging outlets multiple times larger than their size, as is observed on the field (Piton and Recking, 2016).

Typical values for dense gravel are assigned to the particle Young's modulus E, the Poisson coefficient ν, and the coefficient of restitution c. To determine the values of μ_s and μ_r, the procedure presented by Marchelli et al. (2019) is used. In the procedure, each couple of μ_s and μ_r is linked to a single value of the angle of repose, obtained through heap-formation simulations. Specifically, the values used in this work correspond to an angle of repose of about 30°, again a typical value for gravel. Note that the parameters can also alternatively be determined from triaxial tests, as in Cheng et al. (2017).

The DEM simulation environment is illustrated in Fig. 9(b). The simulation geometry is a simplified version of the site in St. Vincent. A rectangular channel is built using flat, frictional walls with constant friction angle $\phi = 30°$ at the bottom and at the sides. The channel is inclined at a constant angle of 12°. To keep runtime reasonable, the channel width is reduced to 4.2 m, corresponding to eight metal bars. Only the central part of barrier and flow is therefore simulated. The channel length is also reduced to 10.0 m.

The granular mass representing the flow front is set up by generating a debris sample within a partition of dimensions 5.0 m × 4.2 m, respectively in the x and y directions (see the inset in Fig. 9(b)). All particles are released at the simulation start with a uniform velocity v_f. The mean grain radius can be either $D = 0.16$ m, 0.20 m, or 0.25 m. These are typical sizes for the grains that clog the barrier at the St. Vincent site. The three samples feature grains that exhibit different size ratio with respect to the outlet size: $S/D \simeq 3.0$, 2.5, and 2.0, respectively. These also correspond to different behaviors when the grains flow through the outlets. The largest grains ($S/D \simeq 2.0$) clog the outlets quickly, while the smallest ($S/D \simeq 3.0$) have a lower probability to jam. Using the small grains, much more material flows downstream before the system stabilizes (Marchelli et al., 2019). In all samples, a 10% dispersity in the radius is included to avoid excessive granular crystallization (Bi et al., 2005).

The barrier is placed at a distance of 0.5 m from the partition that contains the grains, see Fig. 9(b). It mimics the one in St. Vincent, with certain geometrical simplifications. The

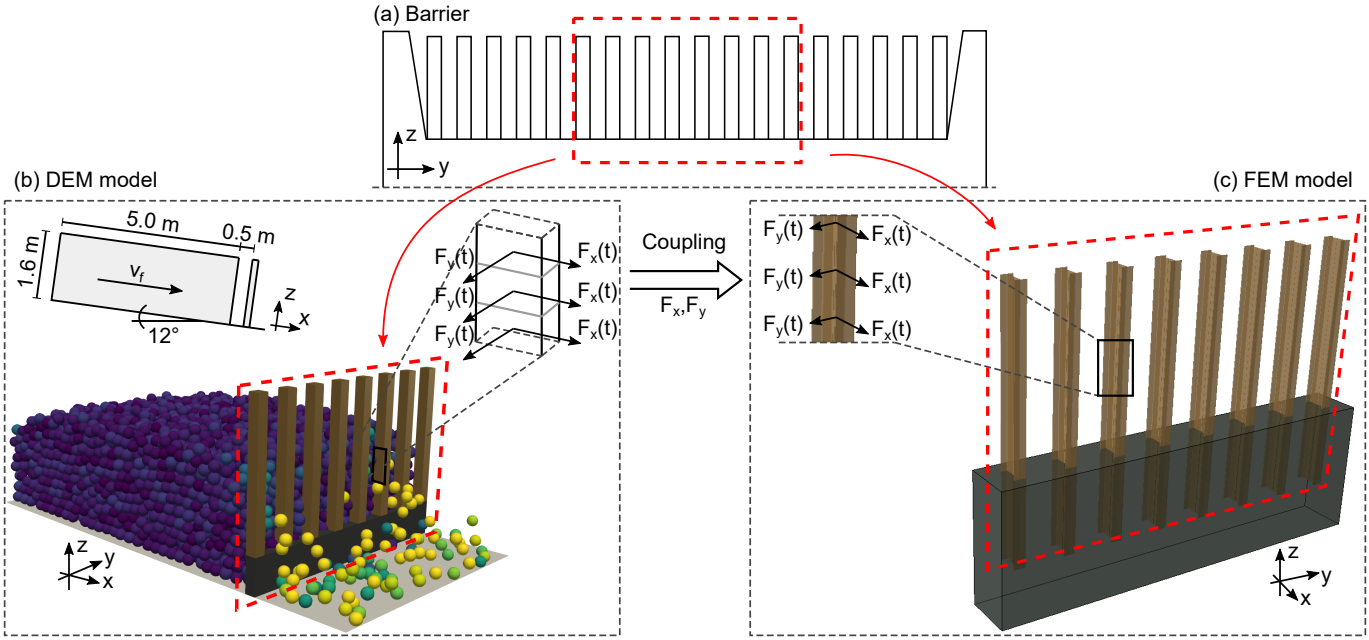

Figure 9: Illustration of workflow used in the numerical framework. The central portion of the barrier (a) is reproduced in the DEM model (b), where it interacts with the flow. The time-history of interaction forces generated in the DEM simulation is transferred to the FEM model (c) where it is used as an external load for a dynamic analysis.

forces acting on the steel bars are the most relevant for the back-calculation of the sensor recordings. However, the concrete basement can have an important function in activating basal and internal friction, and therefore also needs to be represented, at least partially. In total, we represent the uppermost 0.5 m of the concrete basement, and the integrity of the steel bars protruding from it, see Fig. 9 (c).

In the simulations, the barrier is generated by assembling overlapping spheres which can be hit by the moving grains, exchanging momentum. The spheres have elastic properties, but their center of mass is fixed. Thus, nonlinearities due to the barrier deformability are not taken into account in the DEM simulations. This technique allows to compute contact forces between debris and barrier using the same algorithm that tracks the collisions between pairs of moving grains.

The time-history of loads transmitted by the flow during the DEM simulations is collected, in both streamwise ($F_x(t)$) and spanwise ($F_y(t)$) direction, with a sampling rate of 1000 Hz. Each bar is divided into 15 segments, where the resulting load time-history is recorded (see Fig. 9). Therefore, a DEM analysis yields 15 records per bar, corresponding to sections at a different height z along the vertical.

4.2. FEM model for the dynamic response of the barrier

In order to compare the numerical results with the site recordings, the impact load needs to be converted into a strain field in the bars. To do so, we employ a numerical framework: ABAQUS, a FEM solver. In this environment, only the barrier is represented explicitly, while the flow action is introduced as an external load. The model is illustrated in Fig.9 (c). The concrete basement is reproduced using 3D brick elements. The steel frames are modelled as simple 1D beam elements, whose cross section is the IPE 270 profile, as in the field. The beams, as in the actual barrier, are embedded in the concrete basement for 1 m. They are therefore 3 m long in total, with 2 m exposed to the flow. In ABAQUS, the beams and the basement are connected using embedded constraints for the translational degrees of freedom. These are spring-like links with stiffness proportional to those of the connected materials (Tabatabaei et al., 2014). The beams' rotational degrees of freedom are instead simply locked within the basement. At the model sides and bottom, the concrete basement is fully constrained.

Table 3: Geometry and characteristic parameters used for the FEM back-calculation of the structural response.

FEM parameters (barrier)		
Material	Concrete	Steel
Density ρ [kg/m^3]	2500	7850
Young's modulus E [Pa]	$3.0 \cdot 10^{10}$	$2.1 \cdot 10^{11}$
Poisson ratio ν	0.15	0.3
Damping factor α [-]	100	100
Damping factor β [-]	$1.0 \cdot 10^{-8}$	$1.0 \cdot 10^{-8}$

The barrier structural response is obtained though dynamic transient analyses. The FEM model is coupled to the DEM by plugging in the time-histories of forces recorded by the DEM as external point loads on the beams (Fig.9). This technique is in line with similar DEM-FEM models found in the literature. One example is the work by Elmekati and Shamy (2010), who simulated soil-structure interaction by reproducing a small portion of the soil domain using DEM, and the remaining part with a FEM continuum. Similarly, Nakashima and Oida (2004) performed simulations of interaction between soil and an external load source using a DEM-FEM framework.

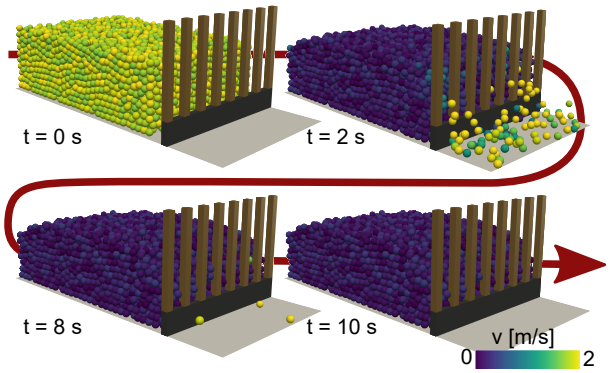

Figure 10: Representation of the impact mechanisms that reconstructs the debris flow front that impacted the barrier on the 9th of June.

Table 4: Geometry and characteristic parameters used for the DEM back-calculation of the event of the 9th of June.

DEM parameters (flow)			
Particle type	Small	Medium	Large
Particle diameter D [m]	0.167	0.200	0.250
Outlet size S/D [-]	3	2.5	2
Particle number	7396	4131	2098
Particle density ρ [kg/m^3]		2630	
Young's modulus E [Pa]		$1.2 \cdot 10^9$	
Poisson ratio ν [-]		0.3	
Restitution coefficient c [-]		0.8	
Friction coefficient μ_s [-]		tan(30°)	
Rolling coefficient μ_r [-]		0.07	
Tangential damping α_t [-]		0.5	

The material parameters for all FEM simulations are constant and listed in Table 3. Their definition is standard in terms of FEM modeling, and all simulations are performed in the linear elastic regime. The stress-strain pattern, and its evolution over time, is obtained by running linear explicit dynamic analyses with a central-difference scheme (as in Liao and Liu, 2017). The Rayleigh damping factors however cannot be easily determined directly (Baillargeon et al., 2004). They should also take into account the damping contribution of the surrounding fluid, which is significant since the bars are almost encircled by debris. This is one of the strongest limitations of this work. The coupling algorithm transfers information in one direction only. Impact forces are transmitted from DEM to FEM, but information on the barrier deformation is not transferred back from FEM to DEM. In order to bypass this issue, the structure is overdamped (see Table 3). In any case, under impact load the maximum and minimum stresses are scarcely affected by a change in these values (Chopra, 2017), as confirmed by our tests and by similar studies in the literature (Kiakojouri and Sheidaii, 2018). As an output of each dynamic analysis, we obtain a time-history of strain distributions along the barrier. This includes strains in the location on the bars that is equivalent to where the extensometers are mounted in the field. Therefore, the two datasets are comparable.

The described numerical setup is used in the following sections with a twofold goal. Firstly, we validate the approach by back-calculating the measurements obtained during the June 9th event in St. Vincent (Fig. 7). Secondly, the approach is used to test the performance of the barrier over a sequence of surges, as prescribed by the Austrian guidelines ONR 24801, and those used in Hong Kong (Kwan, 2012).

5. Back-calculation of field measurements

When the debris flow that generated the set of recordings shown in Fig. 7 happened, a team of technicians was operating in the area. From an analysis of the amateur video recorded in that instance, we know with rough precision the kinematics of the flow that impacted on the barrier. The front velocity was close to $v_f = 2$ m/s, and the flow front had a thickness that peaked at 3/4 of the beam height. Before the event, the basin was only marginally filled with debris.

Using the procedure described in the previous section, we perform a back-calculation of the event. The numerical parameters used in the DEM simulations are listed in Table 4. To follow up from the field observations, we release three granular samples onto the barrier at a uniform velocity of $v_f = 2.0$ m/s, and with maximum thickness 1.6 m. The samples feature particles with different diameters, and different interaction mechanisms when hitting the barrier. The results from the smallest diameter are illustrated in Fig. 10. After an initial momentous impact, the debris flows through the outlets for a time span that depends on the ratio between the outlet size and the mean grain diameter, S/D. For the smallest particles, a stable static configuration is reached after 10 s. Conversely, the large grains clog almost immediately (< 1 s).

For an analytical estimation of the overall load, the dynamic formula (as in Eq. 1) is used here, assuming a unitary empirical coefficient ($k = 1$). In this approach, the expected impact force F^* and bending moment M^* on a bar can be computed using the velocity-dependent impact pressure q_d multiplied by the area of influence of a single bar:

$$F^* = \rho_b v_f^2 i H_B \tag{4}$$

$$M^* = 0.5 \rho_b v_f^2 i H_B^2 \tag{5}$$

where v_f is the front speed used in the simulation, H_B is the bar height, and i the bar spacing (see Fig 4). The bulk density of the debris, ρ_b, is computed as $\rho_b = \rho\phi$, where ρ is the grain mass density from Table 4, and ϕ is the solid volume fraction, assumed to be constant and equal to $\phi = 0.6$, a typical value for monodisperse grains in a dense packing (Choi et al., 2016).

In the simulations, the forces exchanged between flow and barrier are recorded along the bars. The outcome of this process is shown in Fig. 11. In the figure, each plot illustrates a different simulation, i.e. a different dimensionless outlet size S/D. Within each plot, the points represent impulsive forces exerted on the barrier by the flow, divided by the reference force F^* computed with Eq. 4. The forces are illustrated using circular coordinates, where the radial direction represents the magnitude

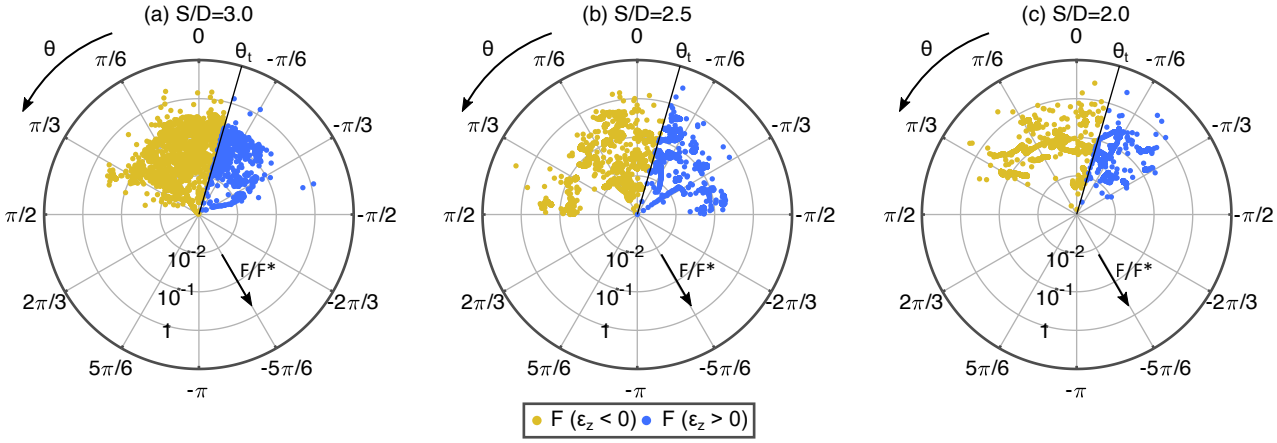

Figure 11: Scaled impact forces, F/F^*, recorded at different levels on the bars. One point every 10 samples is shown, for clarity. Each plot illustrates the results obtained with a different granular assembly, therefore with a different mean grain diameter.

of the impact:

$$F = \sqrt{F_x^2 + F_y^2} \tag{6}$$

and the circular coordinate θ is the angle of incidence, as illustrated in Fig. 6 and defined by:

$$\theta = \text{atan}\left(\frac{F_y}{F_x}\right) \tag{7}$$

If a quasi-static approach is used, each impact generates a shear F and a bending moment $M = F \times H$ at the section where the experimental sensor is located, where H is the height difference between the location of the impact and the location of the sensor, as illustrated in Fig 6. Rewriting Eq. 3, it is evident that a moment M can generate either positive or negative strains, depending on the angle of incidence θ:

$$\varepsilon_z = -\frac{M}{E}\left(\frac{s_y \sin\theta}{I_{yy}} + \frac{s_x \cos\theta}{I_{xx}}\right) \tag{8}$$

In this simplistic view, there is a threshold angle θ_t that determines whether the impact generates positive or negative strains. This is a simple function of the bar section and of the location of the sensor, as provided below:

$$\theta_t = \text{atan}\left(-\frac{I_{xx} s_y}{I_{yy} s_x}\right) \tag{9}$$

The initial particle velocity is aligned with the channel and therefore orthogonal to the barrier. Nevertheless, the impacts reported in Fig. 11 have a wide range of angles of incidence. The majority of high-magnitude impacts are located at around $\theta = 0$. However, a significant portion of strong events are reported over the whole range $-\pi/3 < \theta < \pi/3$.

About 30% of the impacts have an angle of incidence $\theta > \theta_t$. These bend the bars in a direction that results in traction of the sensors ($\varepsilon_z > 0$). These are shown in Fig. 11 with dark color (blue), while those generating compression ($\varepsilon_z < 0$) are reported in a light color (yellow). Conversely the simple orthogonal load model shown in Fig. 5(a), would determine an angle of incidence always equal to $\theta = 0$, thus oversimplifying what is observed in reality.

In order to compare the field measurements with the simulations, the set of load time-histories on the bars are plugged into the FEM model onto the beams, using the procedure described in the previous section. Through the dynamic analyses, the external loads are thus converted into full time histories of strain/stress fields. In particular, the time-histories of resultant moments M_n on each beam at the section where the sensor is located can be computed.

From the results of the simulations, it is clear that the angle of incidence significantly influences the strain measured by the sensor. Unfortunately, this implies that every value of ε_z recorded in the field can be obtained with multiple combinations (M_s,θ_s). The measurements, therefore, cannot be exclusively associated to unique values of bending moment.

No quantitative comparison can therefore be carried out between field data and simulations. However, we may check whether the simulations yield results that are compatible with the field data. This procedure is illustrated in Fig. 12, using the same plot style adopted for Fig. 11. We first extract the maximum and minimum strains recorded by every bar during the June 9th event: $\varepsilon_{z,\max}$ and $\varepsilon_{z,\min}$, respectively. Typically, $\varepsilon_{z,\max}$ is positive, and $\varepsilon_{z,\min}$ is negative. Each of these values can be induced by multiple couplets (M_s, θ_s). These are plotted as loci of points (lines) in Fig. 12, and compared with the moments obtained with the DEM-FEM simulation procedure. In particular, they are compared with those moments that induce the maximum and minimum strain in the bars at the sensor location. Before extracting the maximum and minimum numerical moment, the simulation data is re-sampled at 0.87 Hz, which is the sampling frequency of the strain gauges on site. In this way, experimental and numerical datasets become comparable.

Fig. 12 shows that the simulation results are fully compatible with the field recordings. In other words, the type of load obtained in the simulations results in a strain pattern on the barrier that exhibits the same features observed in the field. In particular, both tension and compression values are recorded. Around the area of the graph that corresponds to the prediction

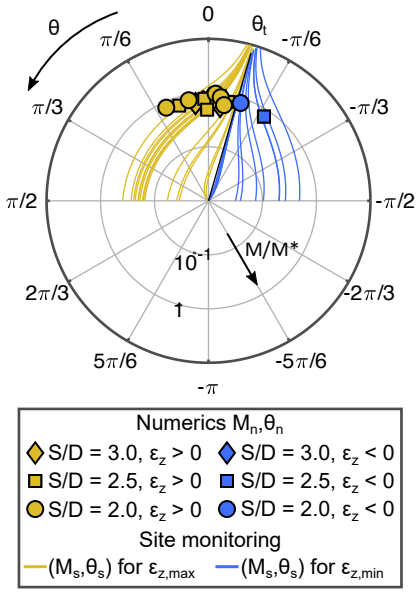

Figure 12: The maximum bending moments computed with the FEM-DEM simulations on the section corresponding to the locations of the field sensors M_n, and corresponding angles of incidence θ_n. This is compared to lines representing the combinations of bending moment M_s and angle of incidence θ_s that correspond to the maximum and minimum strains ϵ_z recorded by the extensometers.

given by the dynamic formula, $M/M^* = 1$, the numerical angles of incidence correspond to those from the site recordings, i.e. in the range $-\pi/12 < \theta < \pi/12$ for large values of S/D and $-\pi/6 < \theta < \pi/6$ for small values.

6. Performance under multi-surge load

From the results of the previous section, it emerges that an orthogonal load model is not always appropriate for the design of such structures. We thereby explore the consequences of the alternative load model provided by the DEM simulations.

Following the load setups suggested by the Austrian and Hong Kong guidelines, a multi-surge process is simulated.

Table 5: Geometry and characteristic parameters used for the multi-stage DEM simulations.

DEM parameters (flow)			
Particle type	Small	Medium	Large
Particle diameter D [m]	0.167	0.200	0.250
Outlet size S/D [-]	3	2.5	2
Particle number (stage 1)	11200	5888	3211
Particle number (stage 2)	12272	6414	3211
Particle number (stage 3)	22437	12008	6630
Particle density ρ [kg/m^3]		2630	
Young's modulus E [Pa]		$1.2 \cdot 10^9$	
Poisson ratio ν [-]		0.3	
Restitution coefficient c [-]		0.8	
Friction coefficient μ_s [-]		tan(30°)	
Rolling coefficient μ_r [-]		0.07	
Tangential damping α_t [-]		0.5	

Three simulations are performed for each particle type. The initial setup for each simulation is illustrated in Fig. 13, and the DEM simulation parameters are gathered in Table 5. Stage 1 corresponds to a single surge of thickness comparable to the barrier height. Stage 2 represents a later surge impacting a barrier which has been partially filled by the deposit left by a previous surge. Stage 3 describes a surge that approaches a filled barrier. In the latter case, the total flow level surpasses the barrier height, causing significant overflow, as in Faug et al. (2011). For each stage, the initial velocity of the surge particles is fixed at $v_f = 2.0$ m/s, as in the simulations presented in the previous section. The remaining particles, constituting the deposit resulting from the precedent stages, are free to move but have zero initial velocity.

This setup therefore reconstructs a typical multi-surge event. It does not, however, describe the limit situation under which the barrier in St. Vincent is supposed be functional, which corresponds to similar flow thicknesses (and surge sequences), but higher velocities (up to $v_f = 5.0$ m/s). Therefore, it is expected that the barrier remains within the elastic limit, and that the surges described by the three stages do not induce irreversible deformations to the structure.

The load exerted during the three DEM stages is concatenated, and plugged into the FEM model. The FEM simulations thus yield the time-history of stresses on the barrier during the whole multi-surge process. The FEM parameters (collected in Table 3) do not differ from those used in the previous sections.

The maximum bending moments at the base of each bar are shown in Fig. 14 for each stage, and each dimensionless outlet size S/D. Stage 3 induces the highest load, even though the surge flows over an almost entirely filled barrier, directly hitting the bars only at the very top. This is consistent with the observations concerning the premature failure of the dam in St. Vincent in 2014. The surge that caused the collapse flowed over a barrier that had already been partially clogged with material from a precedent event.

To compare the performance of the barrier with respect to structural integrity, we compute the moment of first plastic deformation M_{yield} as a function of the angle of incidence θ:

$$M_{\text{yield}} = -\sigma_{\text{yield}} \Big/ \left(\frac{h_y \sin\theta}{I_{yy}} + \frac{h_x \cos\theta}{I_{xx}} \right) \tag{10}$$

where h_x and h_y are the IPE 270 section dimensions (see Table 2). The admissible bending moment is much smaller if the bar is transversely loaded, due to the large difference in the inertia moment in that direction (I_{yy}) with respect to inertia around the strong axis (I_{xx}).

From the DEM-FEM simulations, we extract, for each bar, the combinations of M and θ that lead to the largest absolute values of ε_z on the bar. These values are compared to the maximum admissible moment M_{yield}, of the IPE 270 section, as computed using Eq. 10 (see Fig. 14). Within simulations with similar geometrical configurations (i.e. same stage) the results vary with respect to the S/D ratio. Larger particles induce a slightly higher load than smaller ones, as expected. Moreover, they induce loads with a much larger angle of incidence θ. This is due to the higher probability of jamming, which increases sharply

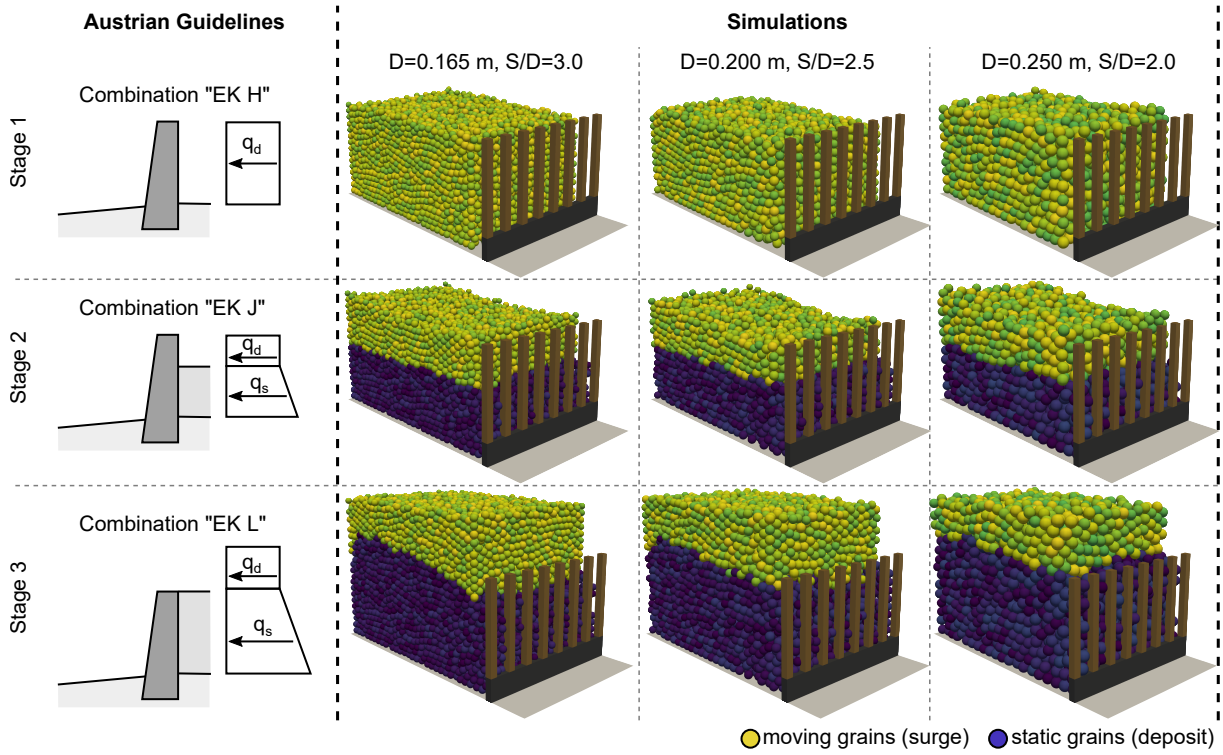

Figure 13: Graphical illustration of the initial setup used for the multi-stage simulations. The three surge configurations are inspired by the Austrian guidelines ONR 24801, an extract of which is reported in the left column. In the guideline load combinations, static grains deposited after precedent events exert a static load q_s on the barrier, while surging grains exert a dynamic load q_d.

with S/D (Marchelli et al., 2019). If jamming occurs rapidly, dynamic impact forces are transferred though granular arches early on, with significant self-balanced transverse loads.

From Fig. 14, it appears that the simulations with the largest particles induce a load that causes irreversible deformation of the bars. This, in spite of the front impact speed $v_f = 2$ m/s being significantly lower than the one the barrier was originally designed to withstand ($v_f = 5$ m/s). The outlet clogging induces additional transverse loads on the structural elements, which can contribute to premature failure of the barrier if not taken into account in the design process. This can be easily prevented by employing a section with similar dimension, but with symmetrical stiffness in the two main directions. For example, the use of a square hollow section with a 250 mm width and a 6 mm thickness (HSS 250) would have resulted in the barrier responding to all stages within its elastic limit, see Fig. 14.

7. Conclusions

Barriers that filter the coarsest grains are an effective measure to reduce the hazard associated with debris flows. In this study, we presented results from one barrier of this type, installed in the Italian Alps, and fully equipped with a monitoring system that tracks the deformation of pivotal structural elements. However, the strains recorded on-site are not compatible with the load model that is usually used to design this type of barrier.

The recordings obtained during an event in June 2016 are thus compared to the results obtained with a numerical model. The model couples DEM and FEM, and is therefore able to simulate with a good degree of precision both the surge impact process and the corresponding strain/stress field of the barrier. The results of the simulations are compatible with the field measurements, therefore validating the approach. They further provide valuable additional information on the space distribution of impact forces.

The results highlight how the load pattern on a filter barrier can be different from the one that is suggested by existing guidelines. When the material flows through the outlets, significant momentum is transferred to structural elements, transversely to the main flow direction. From the results of our analyses, we suggest testing the barrier design for additional transverse loads. The barrier should withstand loads characterized by angles of incidence within the $-\pi/3 < \theta < \pi/3$ range. This is particularly relevant if the grains are large with respect to the outlet size. Furthermore, significant transverse components are also recorded when an overflow scenario is simulated, i.e. a case when the surge directly impacts the barrier only marginally. As a general consequence, structural elements should not have a significant difference in stiffness in the streamwise and transverse direction: they should perform well under biaxial bending. This is particularly important for structures that may clog quickly, such as filter barriers with small openings.

For the barrier installed at the experimental site in St. Vincent, and subject to the monitoring campaign, this has been shown to have important implications on the design safety. In

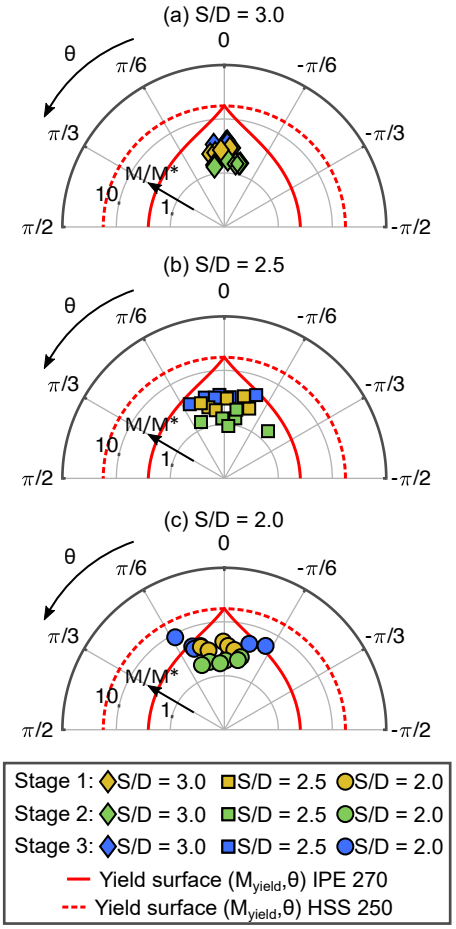

Figure 14: The bending moments giving the most critical conditions on the bars, as reconstructed with the multi-stage DEM-FEM procedure. The yield moment of the bars, as a function of the angle of incidence, is also displayed.

fact, the barrier analyzed hereby was not capable of withstanding the load obtained from the DEM-FEM analysis without incurring in irreversible damage. This alone cannot explain the 2014 collapse, in which even the concrete basement was heavily damaged. However, irreversible damage to the bars can change the bar spacing, therefore altering the filter properties of the barrier. This implies a loss of functionality, which should be avoided.

Finally, the simulations highlight a weak point in the monitoring station used in St. Vincent. In order to effectively monitor the structural response of the barrier, at least two strain gauges per element are necessary. An additional gauge positioned on the opposite flange would record a second value of ε_z, from which both the intensity of the bending moment and the angle of incidence could be unequivocally determined. Such a system would allow a reconstruction of the exact load distribution on the filter elements without a priori assumption.

Acknowledgements

The monitoring system in St. Vincent was funded by the RISKNAT project - Operational programme Italy - France (Alps - ALCOTRA) 2007-2013, the Mhymesis - Modelling Hazard of hYperconcentrated Mountain flows: a wEbgis SImulation System project 2015-2017 and C. Scavia's research funding (Politecnico di Torino). The Authors wish to thank V. Segor, L. Pitet and P. Gaia (Aosta Valley Autonomous Region) as well as M. Barbero, F. Barpi, M. Borri-Brunetto, and O. Pallara (Politecnico di Torino) for the design and configuration of the monitoring system. The authors are grateful to E. Calcagno for his help in generating and processing the FEM model, and to M. Ceccarelli and A. Lombrino for the interpretation of part of the monitoring data. Computational resources were provided by HPC@POLITO, a project of Academic Computing within the Department of Control and Computer Engineering at Politecnico di Torino (www.hpc.polito.it).

References

Albaba, A., Lambert, S., Nicot, F., Chareyre, B., Etgr, U.R., Hères, S.m., 2015. Modeling the Impact of Granular Flow against an Obstacle, in: Wu, W. (Ed.), Recent Advances in Modeling Landslides and Debris Flows. Springer International Publishing Switzerland. Springer Series in Geomechanics and Geoengineering, pp. 95–105. doi:10.1007/978-3-319-11053-0.

Albert, I., Tegzes, P., Kahng, B., Albert, R., Sample, J., Pfeifer, M., Barabasi, A., Vicsek, T., Schiffer, P., 2000. Jamming and fluctuations in granular drag. Physical Review Letters 84, 5122–5125.

Ashour, A., Wegner, S., Trittel, T., Börzsönyi, T., Stannarius, R., 2017. Outflow and clogging of shape-anisotropic grains in hoppers with small apertures. Soft Matter 13, 402–414. doi:10.1039/c6sm02374f.

Baillargeon, B.P., Vel, S.S., Koplik, J.S., 2004. Utilizing ABAQUS to Analyze the Active Vibration Suppression of Structural Systems, in: 2004 ABAQUS Users Conference, pp. 81–94.

Berger, C., McArdell, B.W., Schlunegger, F., 2011. Direct measurement of channel erosion by debris flows, Illgraben, Switzerland. Journal of Geophysical Research: Earth Surface 116, 1–18. doi:10.1029/2010JF001722.

Bharadwaj, R., Wassgren, C., Zenit, R., 2006. The unsteady drag force on a cylinder immersed in a dilute granular flow. Physics of Fluids 18, 043301. doi:10.1063/1.2191907.

Bi, W., Delannay, R., Richard, P., Taberlet, N., Valance, A., 2005. Two- and three-dimensional confined granular chute flows: Experimental and numerical results. Journal of Physics Condensed Matter 17, 2457–2480. doi:10.1088/0953-8984/17/24/006.

Borri-Brunetto, M., Alessio, M., Barbero, M., Barpi, F., De Biagi, V., Pallara, O., 2016. Stiffening effect of bolt-on transducers on strain measurements. Latin American Journal of Solids and Structures 13, 536–553. doi:10.1590/1679-78252109.

Cabrera, M., Estrada, N., 2019. Granular column collapse: Analysis of grain-size effects. Physical Review E 99, 1–7. doi:10.1103/PhysRevE.99.012905.

Calvetti, F., di Prisco, C., Redaelli, I., Sganzerla, A., Vairaktaris, E., 2019. Mechanical interpretation of dry granular masses impacting on rigid obstacles. Acta Geotechnica 9. URL: http://link.springer.com/10.1007/s11440-019-00831-9, doi:10.1007/s11440-019-00831-9.

Canelli, L., Ferrero, A.M., Migliazza, M., Segalini, A., 2012. Debris flow risk mitigation by the means of rigid and flexible barriers experimental tests and impact analysis. Natural Hazards and Earth System Science 12, 1693–1699. doi:10.5194/nhess-12-1693-2012.

Ceccato, F., Redaelli, I., di Prisco, C., Simonini, P., 2018. Impact forces of granular flows on rigid structures: Comparison between discontinuous (DEM) and continuous (MPM) numerical approaches. Computers and Geotechnics 103, 201–217. URL: https://doi.org/10.1016/j.compgeo.2018.07.014, doi:10.1016/j.compgeo.2018.07.014.

Cheng, K., Wang, Y., Yang, Q., 2018. A semi-resolved CFD-DEM model for seepage-induced fine particle migration in gap-graded soils. Computers and Geotechnics 100, 30–51. doi:10.1016/j.compgeo.2018.04.004.

Cheng, K., Wang, Y., Yang, Q., Mo, Y., Guo, Y., 2017. Determination of microscopic parameters of quartz sand through tri-axial test using the discrete element method. Computers and Geotechnics 92, 22–40. doi:10.1016/j.compgeo.2017.07.017.

Chevoir, F., Gaulard, F., Roussel, N., 2007. Flow and jamming of granular mixtures through obstacles. Epl 79, 14001. doi:10.1209/0295-5075/79/14001.

Choi, C.E., Goodwin, G.R., Ng, C.W.W., Cheung, D.K.H., Kwan, J.S.H., Pun, W.K., 2016. Coarse granular flow interaction with slit structures. Géotechnique Letters 6, 267–274. doi:10.1680/jgele.16.00103.

Chopra, A.K., 2017. Dynamics of structures: theory and applications to earthquake engineering. Prentice-Hall.

Coe, J.A., Kinner, D.A., Godt, J.W., 2008. Initiation conditions for debris flows generated by runoff at Chalk Cliffs, central Colorado. Geomorphology 96, 270–297. doi:10.1016/j.geomorph.2007.03.017.

Comiti, F., Marchi, L., Macconi, P., Arattano, M., Bertoldi, G., Borga, M., Brardinoni, F., Cavalli, M., D'Agostino, V., Penna, D., Theule, J., 2014. A new monitoring station for debris flows in the European Alps: First observations in the Gadria basin. Natural Hazards 73, 1175–1198. doi:10.1007/s11069-014-1088-5.

Dai, Z., Huang, Y., Cheng, H., Xu, Q., 2017. SPH model for fluidstructure interaction and its application to debris flow impact estimation. Landslides 14, 917–928. doi:10.1007/s10346-016-0777-4.

Ding, W.T., Xu, W.J., 2018. Study on the multiphase fluid-solid interaction in granular materials based on an LBM-DEM coupled method. Powder Technology 335, 301–314. URL: https://doi.org/10.1016/j.powtec.2018.05.006, doi:10.1016/j.powtec.2018.05.006.

Elmekati, A., Shamy, U.E., 2010. A practical co-simulation approach for multiscale analysis of geotechnical systems. Computers and Geotechnics 37, 494–503. doi:10.1016/j.compgeo.2010.02.002.

Faug, T., Caccamo, P., Chanut, B., 2011. Equation for the force experienced by a wall overflowed by a granular avalanche: Experimental verification. Physical Review E 84. doi:10.1103/PhysRevE.84.051301.

Gabrieli, F., Ceccato, F., 2016. Impact of Dry Granular Flows on a Rigid Wall: Discrete and Continuum Approach. Procedia Engineering 158, 152–157. doi:10.1016/j.proeng.2016.08.421.

Hidalgo, R.C., Lozano, C., Zuriguel, I., Garcimart\'in, a., 2013. Force analysis of clogging arches in a silo. Granular Matter 15, 841–848. doi:10.1007/s10035-013-0451-7.

Huang, Y., Zhang, W., Xu, Q., Xie, P., Hao, L., 2012. Run-out analysis of flow-like landslides triggered by the Ms 8.0 2008 Wenchuan earthquake using smoothed particle hydrodynamics. Landslides 9, 275–283. doi:10.1007/s10346-011-0285-5.

Hübl, J., Suda, J., Proske, D., Kaitna, R., Scheidl, C., 2009. Debris Flow Impact Estimation, in: International Symposium on Water Management and Hydraulic Engineering, Ohrid/Macedonia. pp. 137–148.

Hungr, O., Evans, S.G., Bovis, M.J., Hutchinson, J.N., 2001. A Review of the Classification of Landslides of the Flow Type. Environmental and Engineering Geoscience 7, 221–238.

Hungr, O., Jakob, M., 2005. Debris-flow Hazards and Related Phenomena. Springer-Verlag Berlin Heidelberg. doi:10.1007/b138657.

Hürlimann, M., Abancó, C., Moya, J., Raïmat, C., Luis-Fonseca, R., 2011. Debris-Flow Monitoring Stations in the Eastern Pyrenees . Description of Instrumentation, First Experiences and Preliminary Results. Italian Journal of Engineering Geology and Environment , 553–562doi:10.4408/IJEGE.2011-03.B-061.

Hürlimann, M., Rickenmann, D., Graf, C., 2003. Field and monitoring data of debris-flow events in the Swiss Alps. Canadian Geotechnical Journal 40, 161–175. doi:10.1139/t02-087.

Iverson, R.M., 2015. Scaling and design of landslide and debris-flow experiments. Geomorphology 244, 9–20. doi:10.1016/j.geomorph.2015.02.033.

Janda, A., Zuriguel, I., Garcimartín, A., Pugnaloni, L.A., Maza, D., 2008. Jamming and critical outlet size in the discharge of a two-dimensional silo. Epl 84. doi:10.1209/0295-5075/84/44002.

Kaitna, R., Palucis, M.C., Yohannes, B., Hill, K.M., Dietrich, W.E., 2016. Effects of coarse grain size distribution and fine particle content on pore fluid pressure and shear behavior in experimental debris flows. Journal of Geophysical Research: Earth Surface 121, 415–441. doi:10.1002/2015JF003725.

Kiakojouri, F., Sheidaii, M.R., 2018. Effects of finite element modeling and analysis techniques on response of steel moment-resisting frame in dynamic column removal scenarios. Asian Journal of Civil Engineering 19, 295–307. URL: https://doi.org/10.1007/s42107-018-0027-2, doi:10.1007/s42107-018-0027-2.

Kogelnig, A., Hübl, J., Suriñach, E., Vilajosana, I., McArdell, B.W., 2014. Infrasound produced by debris flow: Propagation and frequency content evolution. Natural Hazards 70, 1713–1733. doi:10.1007/s11069-011-9741-8.

Koo, R.C., Kwan, J.S., Lam, C., Ng, C.W., Yiu, J., Choi, C.E., Ng, A.K., Ho, K.K., Pun, W.K., 2017. Dynamic response of flexible rockfall barriers under different loading geometries. Landslides 14, 905–916. doi:10.1007/s10346-016-0772-9.

Kwan, J., 2012. Supplementary Technical Guidance on Design of Rigid Debris-resisting Barriers. Technical Report 270. Geotechnical Engineering Office. Hong Kong.

Kwan, J., Koo, R., Ng, C., 2015. Landslide mobility analysis for design of multiple debris-resisting barriers. Canadian Geotechnical Journal 52, 1345–1359. doi:10.1139/cgj-2014-0152.

Leonardi, A., Goodwin, G.R., Pirulli, M., 2019. The force exerted by granular flows on slit dams. Acta Geotechnica in press. doi:10.1007/s11440-019-00842-6.

Leonardi, A., Wittel, F.K., Mendoza, M., Herrmann, H.J., 2015. Lattice-Boltzmann Method for Geophysical Plastic Flows, in: Wu, W. (Ed.), Recent Advances in Modeling Landslides and Debris Flows. Springer International Publishing, Cham. Springer Series in Geomechanics and Geoengineering, pp. 131–140. doi:10.1007/978-3-319-11053-0.

Leonardi, A., Wittel, F.K., Mendoza, M., Vetter, R., Herrmann, H.J., 2016. Particle-Fluid-Structure Interaction for Debris Flow Impact on Flexible Barriers. Computer-Aided Civil and Infrastructure Engineering 31, 323–333. doi:10.1111/mice.12165.

Liao, B.B., Liu, P.F., 2017. Finite element analysis of dynamic progressive failure of plastic composite laminates under low velocity impact. Composite Structures 159, 567–578. URL: http://dx.doi.org/10.1016/j.compstruct.2016.04.012, doi:10.1016/j.compstruct.2016.09.099.

Llano-Serna, M.A., Farias, M.M., Pedroso, D.M., 2016. An assessment of the material point method for modelling large scale run-out processes in landslides. Landslides 13, 1057–1066. doi:10.1007/s10346-015-0664-4.

Luding, S., 2008. Cohesive, frictional powders: Contact models for tension. Granular Matter 10, 235–246. doi:10.1007/s10035-008-0099-x.

Luis-Fonseca, R., Raïmat, C., Hürlimann, M., Abancó, C., Moya, J., Fernández, J., 2011. Debris-flow protection in recurrent areas of the Pyrenees - Experience of the VX systems from output results collected in the pioneer monitoring station in Spain. 5th International Conference on Debris-Flow Hazards Mitigation, Mechanics, Prediction and Assessment" , 1063–

1071doi:10.4408/IJEGE.2011-03.B-115.
Marchelli, M., Leonardi, A., Pirulli, M., Scavia, C., 2019. On the efficiency of slit dams in retaining granular flows. Géotechnique in press. doi:10.1680/jgeot.18.p.044.
Marchi, L., Arattano, M., Deganutti, A.M., 2002. Ten years of debris-flow monitoring in the Moscardo Torrent (Italian Alps). Geomorphology 46, 1–17. doi:10.1016/S0169-555X(01)00162-3.
McArdell, B.W., Bartelt, P., Kowalski, J., 2007. Field observations of basal forces and fluid pore pressure in a debris flow. Geophysical Research Letters 34, L07406. doi:10.1029/2006GL029183.
McCoy, S.W., Kean, J.W., Coe, J.a., Staley, D.M., Wasklewicz, T.a., Tucker, G.E., 2010. Evolution of a natural debris flow: In situ measurements of flow dynamics, video imagery, and terrestrial laser scanning. Geology 38, 735–738. doi:10.1130/G30928.1.
Nakashima, H., Oida, A., 2004. Algorithm and implementation of soil-tire contact analysis code based on dynamic FE-DE method. Journal of Terramechanics 41, 127–137. doi:10.1016/j.jterra.2004.02.002.
Navratil, O., Liébault, F., Bellot, H., Travaglini, E., Theule, J., Chambon, G., Laigle, D., 2013. High-frequency monitoring of debris-flow propagation along the Réal Torrent, Southern French Prealps. Geomorphology 201, 157–171. doi:10.1016/j.geomorph.2013.06.017.
Pastorello, R., Hürlimann, M., DAgostino, V., 2018. Correlation between the rainfall, sediment recharge, and triggering of torrential flows in the Rebaixader catchment (Pyrenees, Spain). Landslides 15, 1921–1934. doi:10.1007/s10346-018-1000-6.
Petley, D., 2012. Global patterns of loss of life from landslides. Geology 40, 927–930. doi:10.1130/G33217.1.
Pirulli, M., Barbero, M., Barpi, F., Borri-Brunetto, M., Pallara, O., 2014a. The contribution of continuum-mechanics based numerical model to the design of debris flow barriers, in: Proceedings of the 7th International Conference on Engineering Mechanics, Structures, Engineering Geology (EMESEG '14). volume 26, pp. 13–21.
Pirulli, M., Barbero, M., Barpi, F., Borri-Brunetto, M., Pallara, O., Segor, V., 2014b. Analisi dell'interazione tra colate detritiche e opere di difesa: il caso del torrente Grand Valey (Valle d'Aosta), in: Atti del XXV Convegno Nazionale di Geotecnica - La geotecnica nella difesa del territorio e delle infrastrutture dalle calamità naturali, pp. 673–680.
Pirulli, M., Pastor, M., 2012. Numerical study on the entrainment of bed material into rapid landslides. Géotechnique , 1–14doi:10.1680/geot.10.P.074.
Piton, G., Recking, A., 2016. Design of Sediment Traps with Open Check Dams. I: Hydraulic and Deposition Processes. Journal of Hydraulic Engineering 142, 04015045. doi:10.1061/(ASCE)HY.1943-7900.0001048.
Pöschel, T., Schwager, T., 2005. Computational granular dynamics: Models and algorithms. Springer. doi:10.1007/3-540-27720-X.
Rudolf-Miklau, F., Suda, J., 2011. Technical standards for debris flow barriers and breakers. Italian Journal of Engineering Geology and Environment , 1083–1091doi:10.4408/IJEGE.2011-03.B-117.
Song, D., Chen, X.Q., Zhou, G.G.D., Zhao, T., Hu, H.S., 2018. Experimental study on the regulation function of slit dam against debris flows. Landslides 16, 75–90. doi:10.1007/s10346-018-1065-2.
Suda, J., Rudolf-miklau, F., Hübl, J., 2012. Design and Maintenance of Torrential Barriers the Austrian Standard Rules Series Onr 24800 , in: 12th Congress INTERPRAEVENT 2012, pp. 24800–24801.
Suwa, H., Okano, K., Kanno, T., 2011. Forty years of debris-flow monitoring at Kamikamihorizawa Creek, Mount Yakedake. 5th International Conference on Debris-Flow Hazards Mitigation , 605–613doi:10.4408/IJEGE.2011-03.B-066.
Tabatabaei, S.A., Lomov, S.V., Verpoest, I., 2014. Assessment of embedded element technique in meso-FE modelling of fibre reinforced composites. Composite Structures 107, 436–446. URL: http://dx.doi.org/10.1016/j.compstruct.2013.08.020, doi:10.1016/j.compstruct.2013.08.020.
Tecca, P.R., Genevois, R., 2009. Field observations of the June 30, 2001 debris flow at Acquabona (Dolomites, Italy). Landslides 6, 39–45. doi:10.1007/s10346-009-0145-8.
Tsuji, Y., Tanaka, T., Ishida, T., 1992. Lagrangian numerical simulation of plug flow of cohesionless particles in a horizontal pipe. Powder Technology 71, 239–250.
Wendeler, C., McArdell, B., 2006. Field testing and numerical modeling of flexible debris flow barriers, in: Proc. Int. Conf. on Physical Modelling in Geotechnics, Hong Kong. p. 15731604.